# In situ generating CO gas for destroying bacterial biofilms

*Pengzhen Zhuang*[1,2], *Wu Yang*[1,2], *Yu Zhang*[1,2], *Yu Chen*[1,2], *Tao Ding*[1], *Yanyang Chen*[1], *Fei Wang*[1], *Jessica Rosenholm*[2,3], *Yingchuan Li*[4]*, *Hongbo Zhang*[1,2,3]*, *Wenguo Cui*[1]*

[1]Department of Orthopaedics, Shanghai Key Laboratory for Prevention and Treatment of Bone and Joint Diseases, Shanghai Institute of Traumatology and Orthopaedics, Ruijin Hospital, Shanghai Jiao Tong University School of Medicine, 197 Ruijin 2nd Road, Shanghai, 200025, PR China

[2]Pharmaceutical Sciences Laboratory, Faculty of Science and Engineering, Åbo Akademi University, Turku, 20520, Finland

[3]Turku Bioscience Centre, University of Turku and Åbo Akademi University, Turku, 20520, Finland

[4]Department of Critical Care Medicine, Shanghai Tenth People's Hospital, Tongji University, School of Medicine, Shanghai, 200072, PR China

**Abstract:** The resistance and impermeability of bacterial biofilms lead to incurable infections. Interference with bacterial respiration is the key to the eradication of bacterial biofilm, but breaking the deep-tissue biofilm barrier to disrupt bacterial respiration still lacks effective means. Here, we report a hydrogel microsphere that disrupts bacterial respiration, supports in situ production of carbon monoxide gas (CO) to enhance the oxygen-depleted environment of biofilms and disrupts the bacterial respiratory chain, eliminating the bacterial biofilm ecotone (BRDMs). Under the specific interaction of α-helical structure and bacterial biofilm, BRDMs rapidly anchored and accumulated on the surface of bacterial biofilm within 8 h. Meanwhile, 8.64 μM CO gas was released in situ under an oxidative stress environment to deeply penetrate the biofilm and continuously destroy bacterial terminal oxidase, block bacterial respiration and finally disintegrate the biofilm. In a model of osteomyelitis, BRDMs disrupt the ecotopic colonization of MRSA biofilms in deep tissues, reduce inflammation, restore internal environmental homeostasis and accelerate tissue regeneration. BRDMs could be designed to remove drug-resistant biofilms from a wide range of deep tissues.

**Keywords:** hydrogel microsphere, bacterial biofilm, bacterial respiration, CO

## 1. Introduction

Persistent bacterial biofilm infections pose a serious threat to human life. Once an infection occurs, bacteria tend to form microbial aggregates at the interface and colonize tissues rather than exist in large numbers as planktonic bacteria [1,2]. Respiratory metabolism drives bacteria to secrete large amounts of extracellular aggregates and form tight biofilms that greatly enhance bacterial survival, including preventing antibiotic penetration, defending against physicochemical shock, and escaping immune cells attack, which further leads to increased and recurrent infections [3]. Currently, the primary treatments for biofilm infections in the clinic are the use of high-dose antibiotics [4] and surgical excision of the lesion, however, high doses of antibiotics can lead to bacterial resistance and serious complications [5]. Although multiple bactericidal strategies have been developed to remove bacterial biofilms, including precision delivery of antibiotics, physical signaling sterilization [6,7], and chemical signaling sterilization [8], biofilm resistance and refractory penetration remain unresolved [9-11]. Therefore, a therapeutic strategy to avoid resistance and to efficient clearance of bacterial biofilm infections needs to be urgently developed.

Respiration drives bacterial biofilm formation and diffusion, the essence of which lies in obtaining energy and occupying ecological niches through redox processes [12]. As a parthenogenic anaerobic bacterium, MRSA can grow in both oxygen-rich and oxygen-depleted environments, and its unique respiration is capable of energy transfer using molecular oxygen or alternative electron acceptors. In biofilms, the oxygen concentration decreases gradually from the outer to the inner layer, and the outer layer bacteria show metabolic activity by directly using oxygen, while the inner layer of the depleted oxygen environment forces bacteria to utilize alternative electron acceptors to transfer electrons from intracellular NADPH to oxygen in the outer layer of the biofilm to obtain energy and show metabolic slowness [13]. Moreover, oxygen limitation leads to an imbalance in the redox state inside the biofilm and bacteria reduce phosphopiridate expression, while high expression of AltA murine protein hydrolase disrupts the cell wall [14], a process that drives the biofilm to increase its specific surface area to obtain oxygen, manifesting as biofilm diffusion [15]. Therefore, blocking

bacterial respiratory metabolism is ideal for achieving no resistance removal of bacterial biofilms.

Terminal oxidases play a crucial role in bacterial respiration, and disruption of terminal oxidases will directly cause bacterial respiratory damage [16-18]. Terminal oxidases are at the end of the respiratory chain and transfer electrons to oxygen and form $H_2O_2$ or $H_2O$ during redox, where cytochrome oxidase provides a large amount of ATP to bacteria based on the reduction of one oxygen molecule to two water molecules using Fe-cytochrome [19, 20]. Carbon monoxide (CO) poisoning is considered as an invisible killer leading to human mortality, mainly because C≡O bonds are more likely to form Fe=C=O with Fe ions than O=O bonds leading to tissue hypoxia [21, 22]. Therefore, CO is equally expected to compete for oxygen to coordinate with Fe ions to inactivate cytochrome oxidase thereby destroying bacterial biofilms. Currently, commonly used biofilm therapeutic drugs are divided into small molecule drugs (β-lactams, tetracyclines and fluoroquinolones, etc.) and large molecule drugs (peptides, proteins, glycans, etc.). However, small-molecule drugs destroy bacterial cell membranes in close relation to their metabolic state, and large-molecule drugs are poorly permeable, neither of which can truly penetrate and destroy bacterial biofilms [6, 7, 23, 24]. Unlike the mode of action of conventional drugs, CO, which competes with oxygen, does not induce bacterial drug resistance. Moreover, CO gas exhibits strong stability in the physiological environment, which allows it to exert therapeutic effects at a distance. Of concern, a major cause of therapeutic failure in bacterial biofilm infections is the low permeability and enrichment of the therapeutic agent within the biofilm, where the ultra-low molecular weight of CO allows it to diffuse freely into the biofilm and induce continuous bacterial intoxication, thereby disintegrating the biofilm and exerting a bactericidal effect. Therefore, the construction of an infection microenvironment-responsive CO release system will provide stronger applicability for respiratory disruption-mediated biofilm clearance strategies.

To develop a biomaterial that can break the deep-tissue biofilm barrier to disrupt bacterial respiration, we proposed a method to enhance the biofilm's oxygen-depleted environment with CO gas to block bacterial respiration. Specifically, we covalently

grafted CORM-401 molecules as carbon monoxide generators (CONPs) with calcium carbonate, covalently grafted the LL37 antimicrobial peptides on the surface of methacrylated gelatin (GelMa), and finally formed BRDMs using a microfluidic device. Our strategy is based on three considerations. First, the positively charged and alpha helical structure of the LL37 antimicrobial peptide recognizes and enriches the biofilm surface while capturing a large number of planktonic bacteria, creating a dense field of bactericidal activity. Second, the acidic and oxidative stress environment of the biofilm activates the release of CO gas from CONPs, which breaks the biofilm barrier and penetrates into the biofilm interior, which enhances the oxygen-depleted microenvironment inside the biofilm and disrupts bacterial terminal oxidases. Third, the improved infection microenvironment restores internal environmental homeostasis and accelerates the tissue healing process. The physicochemical properties and biofilm eco-site disruption function of BRDMs were evaluated *in vitro*. A bone infection model was established, and BRDMs were injected into the bone infection site to study the biofilm clearance effect of BRDMs *in vivo* and its mechanism.

## 2. Results and discussion

### 2.1 In situ generate CO for MRSA biofilm disruption

Schematic 1 shows the preparation of BRDMs with bacterial biofilm removal function, which mainly includes the following key steps: synthesis of $CaCO_3$@CORM-401 nanoparticles (CONPs), preparation of GelMa/CONPs microspheres, and conjugation of LL37 antimicrobial peptide on the microspheres. Further, the amide reaction was applied to link the carboxyl group of CORM-401 and the amino group of $CaCO_3$ to obtain CONPs, as shown in Fig. 1a, b. We utilized calcium carbonate since it has acid-responsive and good osteoconductivity properties that are suitable for the treatment of osteomyelitis caused by MRSA infection, and its abundant surface hydroxyl groups and free calcium provide a large variety of active sites for surface modification and drug loading. As a favorable anti-inflammatory molecule, the introduction of CORM-401 can confer CO-responsive properties to $CaCO_3$ in ROS environment [24, 25, 26], which can be adopted to improve the oxidative

stress microenvironment of bacterial-induced osteomyelitis, while meeting bone regeneration needs. To endow the BRDMs with the ability to capture bacteria, the LL37 antimicrobial peptide was introduced onto the GelMa surface. The LL37 peptide carries a positive charge and can additionally induce pore formation by inserting itself into the surface of bacterial cell membranes [27], thus efficiently capturing and killing the negatively charged bacteria. Finally, a simple and effective microfluidic device was assembled to prepare BRDMs (Fig. S1), which was based on shearing the aqueous phase of GelMa@LL37/CONPs by liquid paraffin oil at a high flow rate to form the microsphere structure, and finally cross-linking GelMa by UV light to stabilize its structure. Compared to conventional hydrogel materials, hydrogel microspheres have the advantages of large specific surface area [28, 29, 30], strong designability and workability [31-34], high water content and similarity to natural extracellular matrix (ECM) for controlled delivery of various cells, drugs and nanoparticles [35, 36] as well as the applicability of minimally invasive injection [37-41].

**2.2 Characterization of *in situ* CO generation**

The overall morphology and particle size of the BRDMs were recorded by optical microscopy and scanning electron microscopy. The hydrogel microspheres exhibited an overall translucent state with a large number of uniformly distributed wrinkles, which was associated with the cross-linked network formed by GelMa. The particle size distribution statistics showed that the average particle size of the BRDMs was 224 μm (Fig. 1e, h), which could be uniformly dispersed in the ultrapure water and passed through the syringe needle smoothly to meet the injectable requirement (Fig. 1d). Further, massive wrinkles on the surface of the hydrogel microspheres could be observed by scanning electron microscope (SEM), which had a large specific surface area. The overall surface of pure GelMa microspheres was smooth, while the surface of BRDMs was rough and had a large distribution of CaCO3@CORM-401 nanoparticles (Fig. 1f, marked with a yellow arrow). It is worth noting that the introduction of calcium carbonate did not destroy the inherent morphological structure of the hydrogel microspheres. The energy spectra showed the presence of C, Ca, S and Mn on the surface of the BRDMs, further confirming the successful introduction

of $CaCO_3$ and CORM-401, as shown in Fig. 1a and 1b. X-ray Diffraction (XRD) patterns also showed that calcium carbonate was successfully introduced into the hydrogel microspheres, and peaks 012, 104, 110, 113, 202, 018 and 116 were confirmed to belong to calcium carbonate [42] (Fig. 1i).

To further verify the successful coupling of CORM-401 with $CaCO_3$, the $CaCO_3$@CORM-401(CONPs) powders at the end of the amide reaction were characterized by X-ray photoelectron spectroscopy (XPS) (Fig. 2a and S2). The presence of Mn and S elements attributed to the CORM-401 molecule confirmed the successful grafting of the CORM-401 molecule on the $CaCO_3$ surface. On the other hand, the optical properties of CONPs nanoparticles were probed by spectroscopic analysis. The UV spectroscopy showed the presence of characteristic peaks at wavelength 226 nm for CORM-401 and no distinct characteristic peaks for $CaCO_3$ (Fig. 2b). The characteristic absorption peaks of CONPs were similar to those of CORM-401, which further demonstrated the successful coupling of CORM-401 molecule with $CaCO_3$. In addition, the IR spectra [43] of 2916 $cm^{-1}$, 2850 $cm^{-1}$, 2510 $cm^{-1}$, 1796 $cm^{-1}$, 875 $cm^{-1}$ and 713 $cm^{-1}$ were confirmed to be attributed to $CaCO_3$ (Fig. 2c). To demonstrate the successful modification of LL37 antimicrobial peptide onto GelMa/CONPs microspheres, we explored the potential between the components. The zeta potential results showed that the surface potentials of $CaCO_3$, CORM-401, CONPs, GelMa, GelMa@LL37 and GelMa@LL37/CONPs were 11.13±0.85 mV, -3.82±1.42 mV, -1.42±0.06 mV, -18.97±0.85 mV,12.5±0.35 mV,1.395±0.73 mV, respectively, which implied that the surface of calcium carbonate nanoparticles showed negative charge after CORM-401 modification and the surface of microspheres showed positive charge after LL37 modification, which was attributed to the positive group exposed by LL37 antimicrobial peptide [44], and further indicated the successful modification of LL37 (Fig. 2d).

The antibacterial functionality of BRDMS depends on the loading degrees of the LL37 and CORM-401. To further clarify the loading degree and loading efficiency of LL37 antimicrobial peptide and CORM-401 molecule, high performance liquid chromatography and inductively coupled plasma (ICP) were employed to detect the

concentration of the LL37 antimicrobial peptide and Mn ions, respectively. As shown in Fig. 2e, the grafting efficiency of LL37 antimicrobial peptide was calculated as 62.4% and the loading degree (antibacterial peptide per microsphere mass) was 5.87% by the integral area and concentration conversion. The content of Mn ions in the supernatant at the end of the amide reaction was 51.36 mg/L, and the grafting efficiency and loading degree of CORM-401 molecules on the surface of $CaCO_3$ were 69.01% and 6.45% (Fig. 2f). It is noteworthy that CORM-401 was able to release CO gas continuously under ROS stimulation. We used $H_2O_2$ to mimic the ROS microenvironment to stimulate CORM-401 molecules to produce CO gas that was highly bound to hemoglobin, and the spectroscopic determination of the binding products showed that under $H_2O_2$ stimulation, CONPs responded rapidly and released CO gas up to 8.64 μM within 5 minutes, while the CO gas concentration released by CORM-401 without $H_2O_2$ stimulation was only 1.30 μM (Fig. 2g). In addition, we evaluated the *in vitro* biodegradation performance of the GelMa@LL37/CONPs microspheres. The weight loss rate of the microspheres exceeded 60% at two weeks and 90% at four weeks (Fig. S3).

**2.3 In situ generation of CO disrupt the MRSA biofilm ecotone**

The key to bacterial ectone destruction consists of three steps: BRDMs adhere to the bacterial biofilm, BRDMs destroy the bacterial biofilm, BRDMs capture free bacteria, and BRDMs kill bacteria. The LL37 antimicrobial peptide is a peptide produced by the innate immune system to resist bacterial infection and has broad-spectrum antibacterial properties. The positively charged LL37 antimicrobial peptide adsorbs negatively charged bacteria and binds to their cell membranes through electrostatic interaction, embedding in bacterial cell membranes and forming pore channels, since its hydrophobic structural domain facilitates the penetration of the phospholipid bilayer, thus causing bacterial death. In order to investigate the bactericidal effect and effective concentration of the LL37 antimicrobial peptide, we set the LL37 dilutions from 0-1000 μg/mL and incubated with $10^6$ CFU/mL MRSA for 8 h. After diluting the bacterial solution, it can be observed that the IC50 bactericidal concentration of LL37 solution is 31.25 μg/mL, and the bactericidal effect is not significantly improved in

the range of 31.25 -125 μg/mL, but the bactericidal effect of LL37 solution 250 μg/mL is obviously 75.81%, and as the concentration continues to increase, the bactericidal effect has not been further enhanced (Fig. 3a). In addition, previous literature has reported that hydrogel microspheres with porous structures can effectively promote bacterial capture and enrichment, so we grafted LL37 onto GelMa microspheres according to the effective concentration of bactericidal and explored the bactericidal effects of Control, GelMa, GelMa@LL37 and GelMa@LL37/CONPs, respectively. The results showed that compared with Control, the GelMa group had a weak bactericidal effect, LL37 had significant bactericidal properties, and notably, GelMa@LL37/CONPs had the strongest bactericidal effect and was more effective in inhibiting bacteria at high concentrations than the rest of the groups (Fig. 3b). The plate counting method was used to count the bactericidal effect of microspheres on MRSA in each group. Compared with the Control group, the growth of MRSA colonies in the GelMa group was not inhibited, and the number of MRSA colonies in the GelMa@LL37, GelMa@LL37/CONPs groups was significantly reduced, indicating that the growth state of MRSA was significantly inhibited, and the inhibition efficiency was 1.2 ± 0.3%, 79.27 ± 3.89%, and 99.99 ± 0.1%, which further proved the excellent bactericidal properties of GelMa@LL37/CONPs (Fig. 3c, f). The survival status of MRSA after treatment in each group was further verified by live-dead staining, in which calcoxanthin labeled live bacteria as green and PI could penetrate the damaged membrane to label dead bacteria as red. As shown in Fig. 3d, the Control and GelMa groups exhibited more green fluorescence and very little red fluorescence, which indicated that the bacteria remained viable. The red fluorescence of GelMa@LL37 and GelMa@LL37/CONPs groups was 81.92 ± 4.37% and 99.64% ± 0.28%, respectively. The green fluorescence was less, indicating that the integrity of the bacteria was damaged and they could not survive.

To demonstrate the capture performance of BRDMs on MRSA bacteria, we labeled the surface of MRSA with green fluorescence using FITC and removed excess dye using PBS washing and centrifugation three times. The $1\times10^7$ FITC-labeled MRSA bacteria were incubated with the three sets of microspheres for 1 h, 4 h, 12 h and 24 h.

The excess bacterial solution was gently removed from the surface using PBS and the fluorescence intensity was recorded using fluorescence microscopy. As shown in Fig. 3e,h, the amount of MRSA on the surface of GelMa was low, and the fluorescence intensity at 24 h had not reached equilibrium. The fluorescence intensity of GelMa@LL37 and GelMa@LL37/CONPs microspheres groups was stronger, where the fluorescence intensity of GelMa@LL37 microspheres group gradually increased and was close to that of GelMa@LL37/CONPs microspheres group at 24 h, while the fluorescence intensity of GelMa@LL37/CONPs microspheres captured bacteria more efficiently and reached saturation at 12 h. It is clear that the higher efficiency of GelMa@LL37/CONPs microspheres in capturing bacteria is related to the high binding ability of LL37 to bacteria, and the bacteria surrounding the nanoparticles in SEM implies that the CONPs on the surface of BRDMs also have the ability to capture bacteria, which may be related to the positive charge of calcium carbonate nanoparticles (11.13 ± 0.85 mV). To further verify the ability of GelMa@LL37/CONPs microspheres to capture bacteria, we measured the zeta potential of GelMa@LL37/CONPs microspheres co-incubated with MRSA bacteria, and the results showed that the zeta potential of MRSA bacterial solution and GelMa@LL37/CONPs was -31.7±2.07 mV and 1.395±0.73 mV, and the zeta potential of MRSA+GelMa@LL37/CONPs microspheres was -24.77±1.01 mV, which indicates that GelMa@LL37/CONPs microspheres captured MRSA and neutralized the strong negative potential on the surface of MRSA bacteria (Fig. 3g). The morphology of MRSA was further observed by scanning electron microscopy. The morphology of bacteria in the GelMa microspheres group was intact and smooth, while the bacteria in the GelMa@LL37, GelMa@LL37/CONPs microspheres groups started to appear deformed and irregular, especially the MRSA in the GelMa@LL37/CONPs microspheres group was wrapped by CONPs which further disrupted its membrane structure (Fig. 4a).

A variety of smart antibiotic delivery vehicles (metal-based carriers [45], inorganic carriers [46, 47], organic carriers [48, 49], and composite carriers [6, 7, 50, 51]) have been developed for the treatment of bacterial infections, but these vehicles only target

infectious biofilms and do not penetrate deeply and clear bacterial biofilms. In recent years, physiologically important gases， including carbon monoxide (CO)[24, 25], nitric oxide (NO) [52], sulfur dioxide ($SO_2$) [53], hydrogen sulfide ($H_2S$) [54], and hydrogen ($H_2$) [55] have been developed as new therapeutics for antimicrobial applications. As the third largest gas messenger small molecule in the human body, endogenous CO can be produced *in vivo* by heme oxygenase (HO) catalyzing the degradation of heme, which has physiological functions such as anti-inflammatory and anti-apoptotic [56]. However, the antibacterial mechanism of CO remains unclear. To investigate the scavenging effect of BRDMs on biofilm, we used laser confocal microscopy to observe the survival state of bacterial biofilm after co-incubation of BRDMs with MRSA bacterial biofilm for 8 h. As shown in Fig. 4b, GelMa microspheres had weak affinity with MRSA biofilm and were easily detached from the biofilm during PBS washing, while GelMa@LL37 microspheres had stronger affinity with the biofilm， and a large number of microspheres could be retained on the biofilm. GelMa@LL37/CONPs BRDMs greatly disrupted the integrity of the bacterial biofilm, and the residual bacteria showed a sparsely distributed patchy pattern. The plate counting method further verified that the GelMa@LL37/CONPs microspheres group had good bacterial biofilm removal. We formed bacterial suspensions by adding PBS and shaking with ultrasound, and recorded OD values at 600 nm using an enzyme marker. The mean OD values of bacteria in GelMa@LL37 and GelMa@LL37/CONPs groups were 1.01 and 0.42, which were significantly less than 1.72 and 1.40 in the Control and GelMa groups (Fig. 4c). In addition, the mean bacterial biofilm thicknesses were 43.47 μm and 39.60 μm for the Control and GelMa groups and 33.00 μm and 4.97 μm for the GelMa@LL37 and GelMa@LL37/CONPs groups (Fig. 4g). Although the introduction of LL37 had some inactivating effect on free bacteria, the removal effect on dense bacterial biofilm was still weak, and the bacterial biofilm hindered the penetration of LL37. Compared to conventional antibiotics, CO gas was able to easily pass through the dense bacterial biofilm and disintegrate the binding between the bacterial biofilm itself and tissue. Further, the survival of bacterial biofilm was assessed using crystalline violet staining (562 nm) and the GelMa@LL37/CONPs

microspheres group had less bacterial biofilm remaining and was significantly different from the rest of the groups (Fig. 4d).

Bacterial respiratory chain damage was assessed in MRSA to investigate the potential bactericidal mechanism of BRDMs. In a bacterial survival environment, respiratory chain dehydrogenase is thought to maintain bacterial viability through hydrogen transfer and electron transfer to produce ATP [57]. Fig. 4e, f demonstrates the respiratory chain dehydrogenase activity and ATP content of MRSA after coincubation with BRDMs for 8 h. Compared to the Control and GelMa, GelMa@LL37 and GelMa@LL37/CONPs groups significantly disrupted the respiratory chain of the bacteria, which led to a decrease in the ATP content required for bacterial energy metabolism and consequently bacterial death. Moreover, the damage to the bacterial respiratory chain was more pronounced in the GelMa@LL37/CONPs group than in the GelMa@LL37 group, which may be attributed to the high affinity of CO and bacterial terminal oxidase. To clarify the mechanism of bacterial biofilm removal by GelMa@LL37/CONPs microspheres, we evaluated the nucleic acid (Fig. S5) and protein leakage (Fig. S6) of bacteria, and the UV spectrophotometer recorded the nucleic acid leakage of hydrogel microspheres treated with MRSA at 262 nm. Compared to the Control, GelMa, nucleic acid leakage of GelMa@LL37 and GelMa@LL37/CONPs groups was significantly higher for all. The OD values of protein leakage of MRSA treated with hydrogel microspheres measured at 560 nm using the BCA kit showed that protein leakage was significantly higher in the GelMa@LL37 and GelMa@LL37/CONPs groups compared to the Control and GelMa groups. In summary, the combined application of LL37 and CORM-401 may have increased gas permeation and disrupted the bacterial membrane structure, which in turn led to the removal of bacterial biofilm. Fig. 4h shows the schematic diagram of bacterial scavenging by GelMa@LL37@CO microspheres.

**2.4 BRDMs alleviate oxidative stress**

BRDMs should be biocompatible as a locally injectable biomaterial for the treatment of osteomyelitis. Therefore, *in vitro* experiments, we evaluated the cell viability and morphology of hydrogel microspheres-treated bone marrow mesenchymal stem cells

(BMSCs). CCK8 results showed that the Control, GelMa, GelMa@LL37 and GelMa@LL37/CONPs groups exhibited good biocompatibility at 1, 3, 5 and 7 days with no significant differences between groups (Fig. 5a). The results of live-dead staining confirmed that the Control, GelMa, GelMa@LL37 and GelMa@LL37/CONPs microspheres groups had a lower number of dead cells and a satisfactory cell survival status (Fig. 5b). On the third day, the actin and nucleus of BMSCs were stained using phalloidin with red fluorescent and DAPI with blue fluorescent, respectively, and the results showed that the cells in the the Control, GelMa, GelMa@LL37 and GelMa@LL37/CONPs microspheres groups could spread normally and extend pseudopods, further confirming the excellent biocompatibility of hydrogel microspheres. As a multifunctional endogenous gas, carbon monoxide gas mainly produced in liver tissues and has excellent performance in relieving oxidative stress, promoting vasodilation and antibacterial [58, 59]. Studies have shown that BMSC treated with low concentrations of CO gas (0-400 μM) show excellent biocompatibility and the ability to promote bone differentiation, but the underlying mechanism between CO and cells remains unclear [60].

BRDMs as a local injectable material for the treatment of osteomyelitis should possess pro-osteogenic capacity under oxidative stress. Therefore, we used $H_2O_2$ to induce oxidative stress in BMSCs and loaded hydrogel microspheres to assess their osteogenic differentiation ability, and BMSCs treated with BRDMs were subjected to ALP and alizarin red staining on day 7 and 14, respectively. The results showed that compared to the Control, GelMa group, GelMa@LL37 and GelMa@LL37/CONPs microspheres groups showed a significant increase in alkaline phosphatase expression, and at day 14, a large amount of minerals was deposited to form calcium nodules in the cell culture plates, and the GelMa@LL37 and GelMa@LL37/CONPs microspheres groups had the largest amount of calcium nodules deposited compared to the rest of the groups (Fig. 5d). OCN is an indicator of late osteogenesis, and to illustrate further validation of the osteogenic differentiation of hydrogel microspheres, we performed OCN immunofluorescence staining on BMSCs on day 7, and combined with the results of skeleton and nucleus co-localization, it can be seen that the

fluorescence intensity was weaker in the Control and GelMa groups, and OCN expression in the GelMa@LL37 and GelMa@LL37/CONPs microspheres groups was stronger, and quantitative data showed that OCN expression in GelMa@LL37 and GelMa@LL37/CONPs microspheres groups was significantly different from other groups (Fig. 5c,e). The PCR results confirmed that GelMa@LL37 and GelMa@LL37/CONPs microspheres groups obviously promoted the expression of mRNAs of osteogenic-related indicators such as COL-I, RUNX2 and OCN, which implied that LL37 and CO gas exhibited positive effects on osteogenic differentiation of BMSCs under an oxidative stress environment (Fig. 5f-h).

**2.5 BRDMs eradicate MRSA biofilms *in vivo***

To evaluate the *in vivo* antimicrobial effect and osteogenic effect of hydrogel microspheres, a rat bone infection model [26] was established to assess the biological effects of hydrogel microspheres (Fig. 6a, b). First, $1\times10^6$ CFU of MRSA bacteria were injected into the bone marrow cavity of rats for infection, and 3 weeks later the wounds were debrided and a 3 mm diameter defect was prepared at the femoral condyle, followed by injection of hydrogel microspheres, where PBS was used as the Control group. 8 weeks later, the samples were taken for the characterization of antibacterial and osteogenic indexes. At 8 weeks, the optical photographs showed severe erosion and sinus tract formation in the Control and GelMa groups, while the defect was still partially unhealed in the GelMa@LL37 microspheres group, and the GelMa@LL37/CONPs microspheres group had a clean appearance and no obvious defects (Fig. 6c and S7). To further verify the bactericidal effect of hydrogel microspheres *in vivo*, we isolated and mechanically fragmented the femoral condylar defect site while diluting the plate using PBS, and the number of colonies was large and not significantly different between the Control and GelMa groups. The GelMa@LL37 microspheres group had less bacterial load than the former, while the GelMa@LL37/CONPs microspheres group had no significant colonization, implying that the combination of LL37 and CO was effective in killing bacteria in tissues and preventing biofilm adhesion, and the quantitative data were consistent with the smear plate results (Fig. 6d-f). The excellent antibacterial properties of BRDMs improve the

oxidative stress environment caused by bacterial infection *in vivo*, which further accelerates the bone healing process. X-rays also confirmed that the Control and GelMa groups were severely eroded and had sparse bone, while the GelMa@LL37 and GelMa@LL37/CONPs microspheres groups had more intact bone tissue and a higher bone density. Micro-CT performed an overall scan of the bone tissue and bone quality analysis, and the GelMa@LL37 and GelMa@LL37/ CONPs microspheres groups showed higher bone volume compared to the other two groups (Fig. 6c). Quantitative results showed that the Control, GelMa had 20.64% and 21.65% BV/TV, significantly lower than GelMa@LL37 and GelMa@LL37/CONPs with 37.74% and 42.61%. The mean bone density in the Control and GelMa groups was 0.23 $g/cm^3$, and 0.21 $g/cm^3$, significantly lower than 0.36 $g/cm^3$ and 0.42 $g/cm^3$ in the GelMa@LL37 and GelMa@LL37/CONPs groups. Tb.Th represents the mean trabecular plate thickness, and Tb.N represents the trabecular number. Compared to the remaining two groups, the mean bone trabecular thickness was higher in the GelMa@LL37 and GelMa@LL37/CONPs microspheres groups, and the bone separation was lower (Fig. 6g-j).

Next, HE and masson staining (Fig. 7a) as well as OCN immunohistochemical staining were used to verify the osteogenic effect of hydrogel microspheres, and Gram staining (Fig. 7b) was used to assess the histological response to bacterial infection *in vivo*. As shown in Fig. 7c, d, the defect sites in the Control and GelMa groups were larger, with clear borders and less new bone tissue growth. Compared with the first two groups, the GelMa@LL37 and GelMa@LL37/CONPs microspheres groups had higher bone density at the defect site and a smaller defect area, implying more new bone tissue. In addition, OCN immunohistochemical staining further illustrated the greater bone formation capacity of GelMa@LL37 and GelMa@LL37/CONPs microspheres, and the quantitative results were consistent with the staining results (Fig. 7c-e). Further, gram staining was commonly used to confirm bacteria. A large number of intracellular bacteria were present in the bone marrow cavity in the Control and GelMa groups, some intracellular bacteria were still visible in GelMa@LL37, and fewer intracellular bacteria were seen in the GelMa@LL37/CONPs microspheres

group (Fig. 7b).

## 3. Conclusion

Disrupting bacterial respiration has significant opportunities for clearing biofilm infections from deep tissues, but breaking through biofilm spatial barriers to direct disruption of bacterial respiration remains difficult. In this work, we synthesized BRDMs that disrupt bacterial respiration by mimicking the oxygen limitation in biofilm diffusion, where CO gas generated in situ breaks through the biofilm physiological barrier and continuously enhances the oxygen-depleted microenvironment inside the biofilm, forcing the breakdown of recalcitrant biofilms. Meanwhile, CO uncouples bacterial aerobic respiration and interferes with bacterial terminal oxidases to organise bacterial access to ATP, which together lead to disruption of the biofilm ecotone. In a rat osteomyelitis model, CO gas disrupted the ecotone colonisation of MRSA biofilms and accelerated the bone healing process. There are still some limitations to this study. Although the CO gas-enhanced biofilm depleted environment disrupted the bacterial respiratory chain and cleared the MRSA biofilm, the safety of the CORM-401 molecule and the dose used still need to be further explored. In addition, as a physiological signalling molecule, the *in vivo* bactericidal mechanism of CO gas including the link between CO gas and bacterial metabolism, and the link between CO gas and immune regulation still needs to be further explored.

## Acknowledgement

Pengzhen Zhuang and Wu Yang contributed equally to this work. This work was supported by the National Key Research and Development Program of China (2020YFA0908200), National Natural Science Foundation of China (81930051), National Natural Science Foundation of China (grant No. 82272245), Shanghai Municipal Health and Family Planning Commission (2022XD055), Research Fellow (Grant No.353146), Project (347897), Solution for Health Profile (336355), and InFLAMES Flagship (337531) grants from Academy of Finland, Finland China Food and Health International Pilot Project funded by the Finnish Ministry of Education

and Culture, and Guangci Professorship Program of Ruijin Hospital Shanghai Jiao Tong University School of Medicine. This study is part of the activities of the Åbo Akademi University Foundation (SÅA) funded Center of Excellence in Research "Materials-driven solutions for combating antimicrobial resistance (MADNESS).

**Author contributions**

Wenguo Cui and Hongbo Zhang conceived and supervised the project. Pengzhen Zhuang and Wu Yang contributed to the writing of the article and the specific experiment. Yu Zhang and Yu Chen provided support for cell experiments. Tao Ding and Yanyang Chen supervised the process of antibacterial experiment. Fei Wang and Jessica Rosenholm corrected grammar in texts and gave advice on writing.

**Declaration of Competing Interest**

The authors declare that they have no known competing financial interests or personal relationships that could have appeared to influence the work reported in this paper.

**Data availability**

Data will be made available on request.

**Reference**


1. X. Lv, L. Wang, A. Mei, Y. Xu, X. Ruan, W. Wang, J. Shao, D. Yang, X. Dong, Small 19 (2022) 2206220.
2. K. Huang, J. Wang, Q. Zhang, K. Yuan, Y. Yang, F. Li, X. Sun, H. Chang, Y. Liang, J. Zhao, T. Tang, S. Yang, Adv. Funct. Mater. 32 (2022) 2204906.
3. Y. Dhar, Y. Han, Engineered Regeneration 1 (2020) 64-75.
4. T. Liu, W. Liu, L. Zeng, Z. Wen, Z. Xiong, Z. Liao, Y. Hu, ACS Appl. Mater. Interfaces. 14 (2022) 41764-41778.
5. Y. Cheng, Y. Zhang, Z. Zhao, G. Li, J. Li, A. Li, Y. Xue, B. Zhu, Z. Wu, X. Zhang, Adv. Mater. 34 (2022) 2206646.
6. K. Huang, W. Liu, W. Wei, Y. Zhao, P. Zhuang, X. Wang, Y. Wang, Y. Hu, H. Dai, ACS Nano 16 (2022) 19491-19508.
7. Y. Li, X. Liu, B. Li, Y. Zheng, Y. Han, D.F. Chen, K.W.K. Yeung, Z. Cui, Y. Liang, Z. Li, S. Zhu, X. Wang, S. Wu, ACS Nano 14 (2020) 8157-8170.
8. L. Su, Y. Li, S. Tian, F. Huang, Y. Ren, C. Yang, H.C. van der Mei, H.J. Busscher, L. Shi, Acta Biomater. 154 (2022) 559-571.
9. L. Wang, J. Yang, X. Yang, Q. Hou, S. Liu, W. Zheng, Y. Long, X. Jiang, ACS Appl. Mater. Interfaces 12 (2020) 51148-51159.
10. Z. Xu, Y. Xia, P. Zhou, J.J. Li, M. Yang, Y. Zhang, Y. Zhang, Y. Xie, L. Li, H. Pan, S. Xu, G. Wang, Chem. Eng. J. 406 (2021) 126821.
11. S. Obuobi, K. Julin, E.G.A. Fredheim, M. Johannessen, N. Skalko-Basnet, J. Control. Release 324 (2020) 620-632.
12. A.J. Martin-Rodriguez, Trends Microbiol. 31 (2023) 120-134.
13. W. Xiu, L. Wan, K. Yang, X. Li, L. Yuwen, H. Dong, Y. Mou, D. Yang, L. Wang, Nat. Commun. 13 (2022) 3875.
14. A.A. Mashruwala, A.V. Guchte, J.M. Boyd, Elife 6 (2017) e23845.
15. J. Jo, K.L. Cortez, W.C. Cornell, A. Price-Whelan, L.E. Dietrich, Elife 6 (2017) e30205.
16. E. Bueno, S. Mesa, E.J. Bedmar, D.J. Richardson, M.J. Delgado, Antioxid. Redox Signal. 16 (2012) 819-852.

17. V.B. Borisov, E. Forte, Biochemistry (Mosc) 86 (2021) 22-32.
18. M.C. Carrasco, K.J. Dezarn, F.S.T. Khan, S. Hematian, J. Inorg. Biochem. 225 (2021) 111593.
19. M. Brischigliaro, D. Badocco, R. Costa, C. Viscomi, M. Zeviani, P. Pastore, E. Fernandez-Vizarra, Front. Cell. Dev. Biol. 10 (2022) 892069.
20. I. Kucera, V. Sedlacek, Microorganisms 8 (2020) 8.
21. J.J. Rose, K.A. Bocian, Q. Xu, L. Wang, A.W. DeMartino, X. Chen, C.G. Corey, D.A. Guimaraes, I. Azarov, X.N. Huang, Q. Tong, L. Guo, M. Nouraie, C.F. McTiernan, C.P. O'Donnell, J. Tejero, S. Shiva, M.T. Gladwin, J. Biol. Chem. 295 (2020) 6357-6371.
22. X. Qu, M. Wang, M. Wang, H. Tang, S. Zhang, H. Yang, W. Yuan, Y. Wang, J. Yang, B. Yue, Adv. Mater. 34 (2022) 18.
23. Z. Shang, S.Y. Chan, Q. Song, P. Li, W. Huang, Research 2020 (2020) 2016201.
24. J. Liu, R.S. Li, M. He, Z. Xu, L.Q. Xu, Y. Kang, P. Xue, Biomaterials 277 (2021) 121084.
25. J. Wu, Z. Meng, A.A. Exner, X. Cai, X. Xie, B. Hu, Y. Chen, Y. Zheng, Biomaterials 276 (2021) 121001.
26. A.J. Smith, R.E. Clutton, E. Lilley, K.E.A. Hansen, T. Brattelid, PREPARE: guidelines for planning animal research and testing, Lab. Anim. 52 (2018) 135-141.
27. L. Lai, W. Zou, Y. Zhang, Y. Tu, S. Li, T. Xin, T. Zhou, S. Xu, P. Zheng, Q. Pan, W. Zhu, Chem. Eng. J. 435 (2022) 135084.
28. Y. Gao, Q. Ma, Smart Medicine 1 (2022) 1.
29. F. Lin, Y. Li, W. Cui, Biomedical Technology 1 (2023) 18-29.
30. Z. Zhao, Z. Wang, G. Li, Z. Cai, J. Wu, L. Wang, L. Deng, M. Cai, W. Cui, Injectable Microfluidic Hydrogel Microspheres for Cell and Drug Delivery. Adv. Funct. Mater. 31 (2021) 2103339.
31. Q. Zhang, X. Wang, G. Kuang, Y. Zhao, Bioact. Mater. 24 (2023) 185-196.
32. G. Kuang, Q. Zhang, Y. Yu, L. Shang, Y. Zhao, Bioact. Mater. 28 (2023) 326-336.
33. G. Kuang, Q. Zhang, Y. Yu, X. Ding, W. Sun, X. Shen, Y. Zhao, Chem. Eng. J.

455 (2023) 140619.
34. L. Yang, W. Yang, W. Xu, Y. Zhao, L. Shang, Chem. Eng. J., 476 (2023) 146797.
35. Y. Du, C. Li, Y. Zhang, W. Xiong, F. Wang, J. Wang, Y. Zhang, L. Deng, X. Li, W. Chen, W. Cui, Research 2022 (2022) 1-17.
36. L. Zhang, B. Zhang, R. Liang, H. Ran, D. Zhu, J. Ren, L. Liu, A. Ma, L. Cai, ACS Nano 17 (2023) 6410-6422.
37. Q. Zhang, X. Wang, G. Kuang, Y. Yu, Y. Zhao, Research 2022 (2022) 9784510.
38. L. Yang, L. Fan, X. Lin, Y. Yu, Y. Zhao, Adv. Sci. 10 (2023) 2304190.
39. Q. Zhang, G. Kuang, H. Wang, Y. Zhao, J. Wei, L. Shang, Adv. Sci. 10 (2023) 2303818.
40. Q. Zhang, G. Kuang, W. Li, J. Wang, H. Ren, Y. Zhao, Nano-micro Lett. 15 (2023) 44.
41. Q. Zhang, G. Kuang, Y. Yu, X. Ding, H. Ren, W. Sun, Y. Zhao, ACS Appl. Mater. Interfaces 14 (2022) 48527-48539.
42. W. Wang, S. Wang, Q. Liu, X. Wang, J. Zhu, H. Luo, S. Ji, Herit. Sci. 10 (2022) 165.
43. M. Wu, Z. Li, Z. Yuan, H. Jiang, Y. Niu, X. Ruan, X. Yan, X. Li, X. Wu, G. He, X. Jiang, Adv. Funct. Mater. 33 (2022) 7.
44. X. Lin, R. Wang, S. Mai, J. Drug Deliv. Sci. Technol. 60 (2020) 102016.
45. J. Wu, F. Li, X. Hu, J. Lu, X. Sun, J. Gao, D. Ling, ACS Central Sci. 5 (2019) 1366-1376.
46. J.J. Aguilera-Correa, M. Gisbert-Garzaran, A. Mediero, M.J. Fernandez-Acenero, D. de-Pablo-Velasco, D. Lozano, J. Esteban, M. Vallet-Regi, Acta Biomater. 154 (2022) 608-625.
47. M. Yang, S. Qiu, E. Coy, S. Li, K. Zaleski, Y. Zhang, H. Pan, G. Wang, Adv. Mater. 34 (2022) 2106314.
48. X. Ding, C. Yang, W. Moreira, P. Yuan, B. Periaswamy, P.F. de Sessions, H. Zhao, J. Tan, A. Lee, K.X. Ong, N. Park, Z.C. Liang, J.L. Hedrick, Y.Y. Yang, Adv. Sci. 7 (2020) 2001374.
49. W.C. Huang, R. Ying, W. Wang, Y. Guo, Y. He, X. Mo, C. Xue, X. Mao, Adv.

Funct. Mater. 30 (2020) 2000644.

50. A.M. Hada, M. Potara, S. Astilean, A. Cordaro, G. Neri, M. Malanga, A. Nostro, A. Mazzaglia, A. Scala, A. Piperno, Carbohydr. Polym. 293 (2022) 119736.
51. S. Shi, Y. Jiang, Y. Yu, M. Liang, Q. Bai, L. Wang, D. Yang, N. Sui, Z. Zhu, Adv. Funct. Mater. 33 (2022) 2210850.
52. Z. Wang, A. Jin, Z. Yang, W. Huang, ACS Nano 17 (2023) 8935-8965.
53. Y. Venkatesh, K.S. Kiran, S.S. Shah, A. Chaudhuri, S. Dey, N.D.P. Singh, Org. Biomol. Chem. 17 (2019) 2640-2645.
54. Y. Zhang, T. Yue, W. Gu, A. Liu, M. Cheng, H. Zheng, D. Bao, F. Li, J.G. Piao, J. Nanobiotechnol. 20 (2022) 1.
55. H. Chen, Y. Guo, Z. Zhang, W. Mao, C. Shen, W. Xiong, Y. Yao, X. Zhao, Y. Hu, Z. Zou, J. Wu, Nano Lett. 22 (2022) 229-237.
56. T.-Y. Wang, X.-Y. Zhu, F.-G. Wu, Bioact. Mater. 23 (2023) 129-155.
57. X. Zhang, C. Yang, K. Yang, ACS Appl. Mater. Interfaces 12 (2020) 361-372.
58. Z. Li, X. Jia, P. Zhang, Z. Guo, H. Zhao, X. Li, C. Wei, Sensor. Actuat. B-Chem. 344 (2021) 130177.
59. H. Yan, J. Du, S. Zhu, G. Nie, H. Zhang, Z. Gu, Y. Zhao, Small 15 (2019) 1904382.
60. J. Li, L. Song, M. Hou, P. Wang, L. Wei, H. Song, Int. J. Mol. Med. 41 (2018) 2297-2305.

# Figures

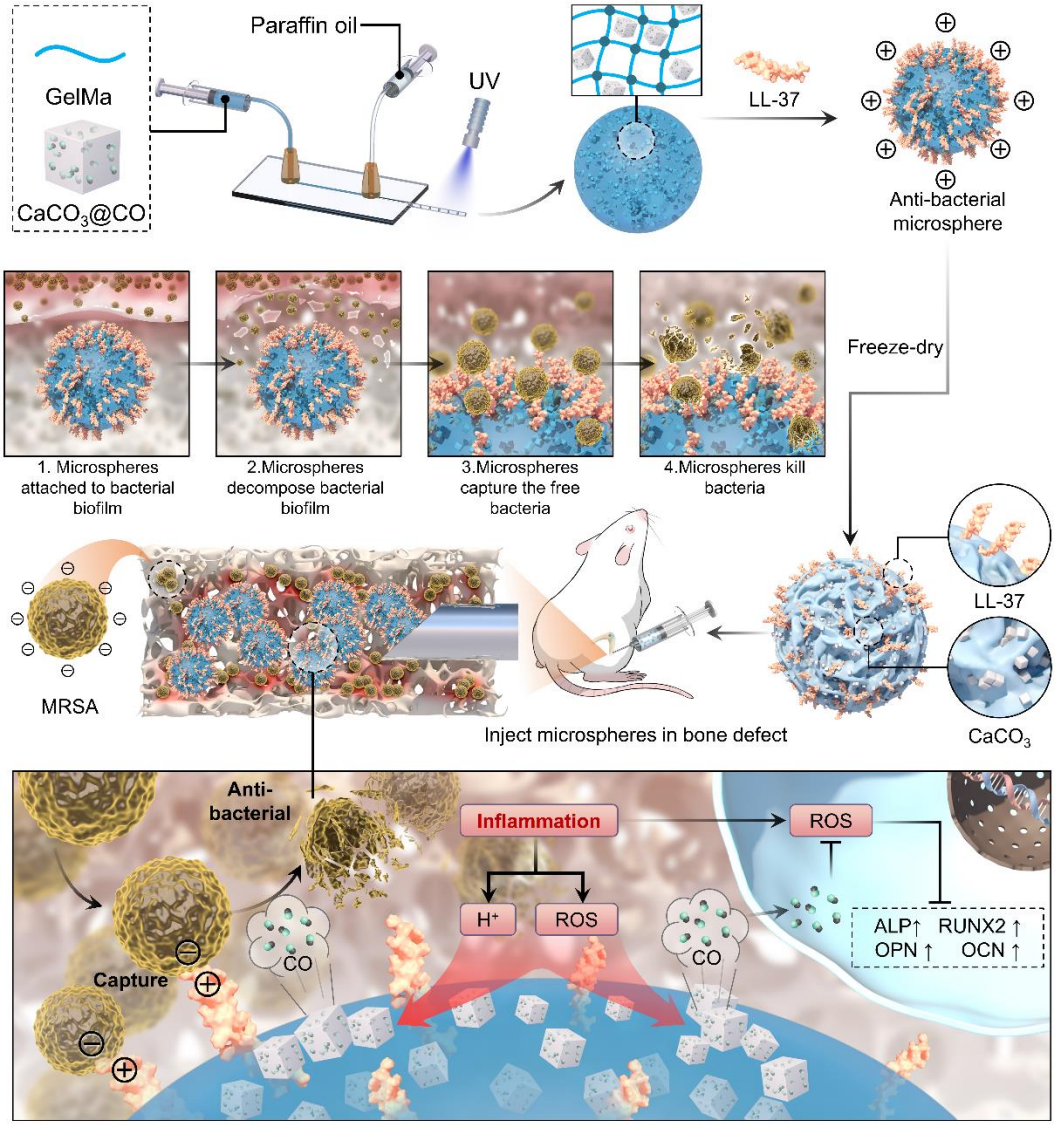


**Schematic 1 In situ generation of CO gas *via* hydrogel microspheres for destroying bacterial biofilms.**

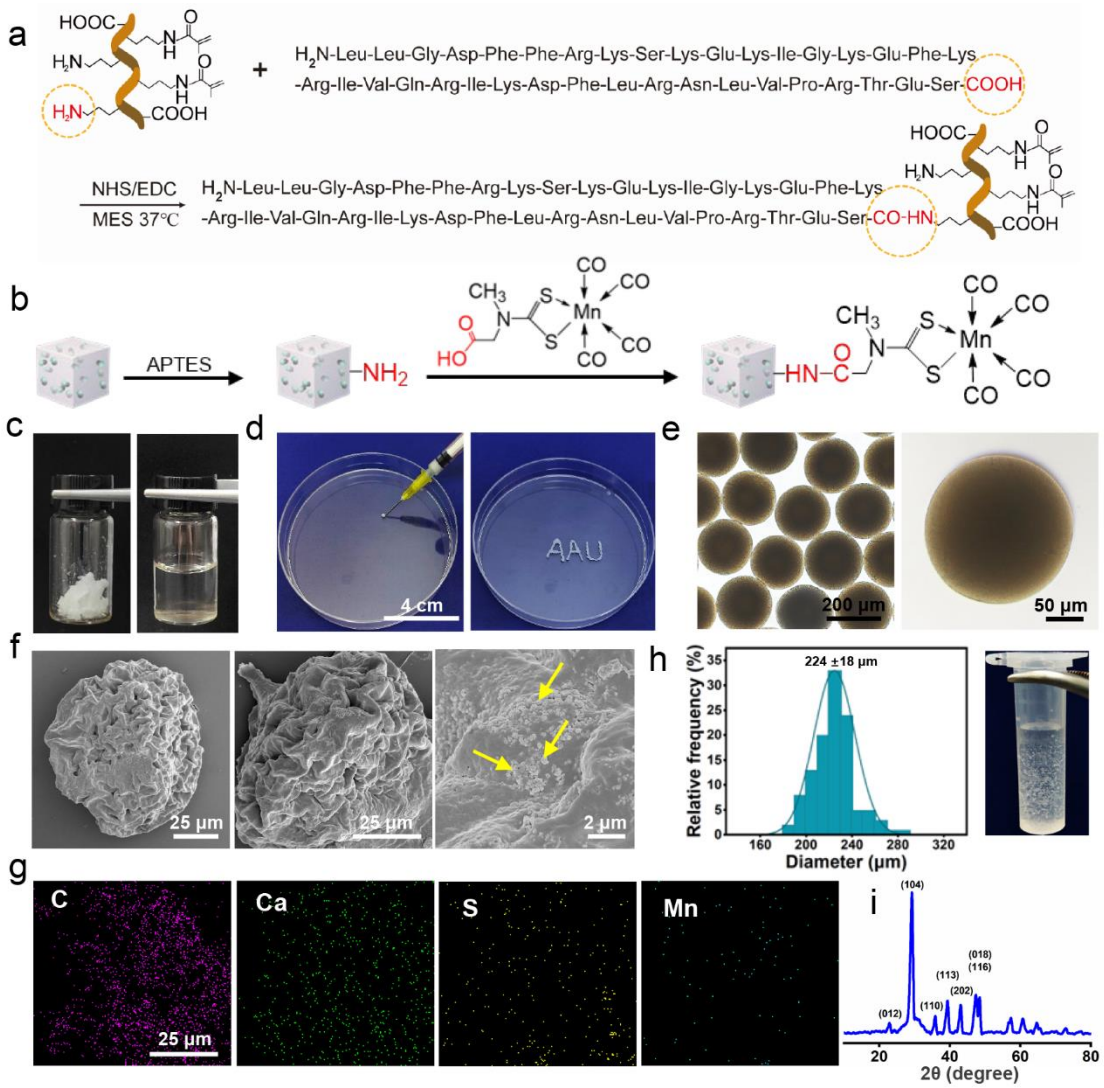


**Fig. 1 Construction of bacterial respiration-disrupting microspheres with in situ release of CO gas. a**,**b**, Schematic diagram of LL37 antimicrobial peptide covalently coupled with GelMa (**a**) and CORM-401 covalently coupled with $CaCO_3$(**b**). **c**, Freeze-dried samples and aqueous solutions of GelMa. **d**, Injectable properties of GelMa microspheres. **e**, Optical microscope images of GelMa microspheres at different magnifications. **f**,**g**, SEM images (**f**) and mapping images (**g**) of GelMa microspheres and GelMa@LL37/CONPs microspheres (the yellow arrows represent CONPs). **h**, Particle size distribution of GelMa@LL37/CONPs microspheres and their dispersion properties in water. **i**, XRD patterns of CONPs.

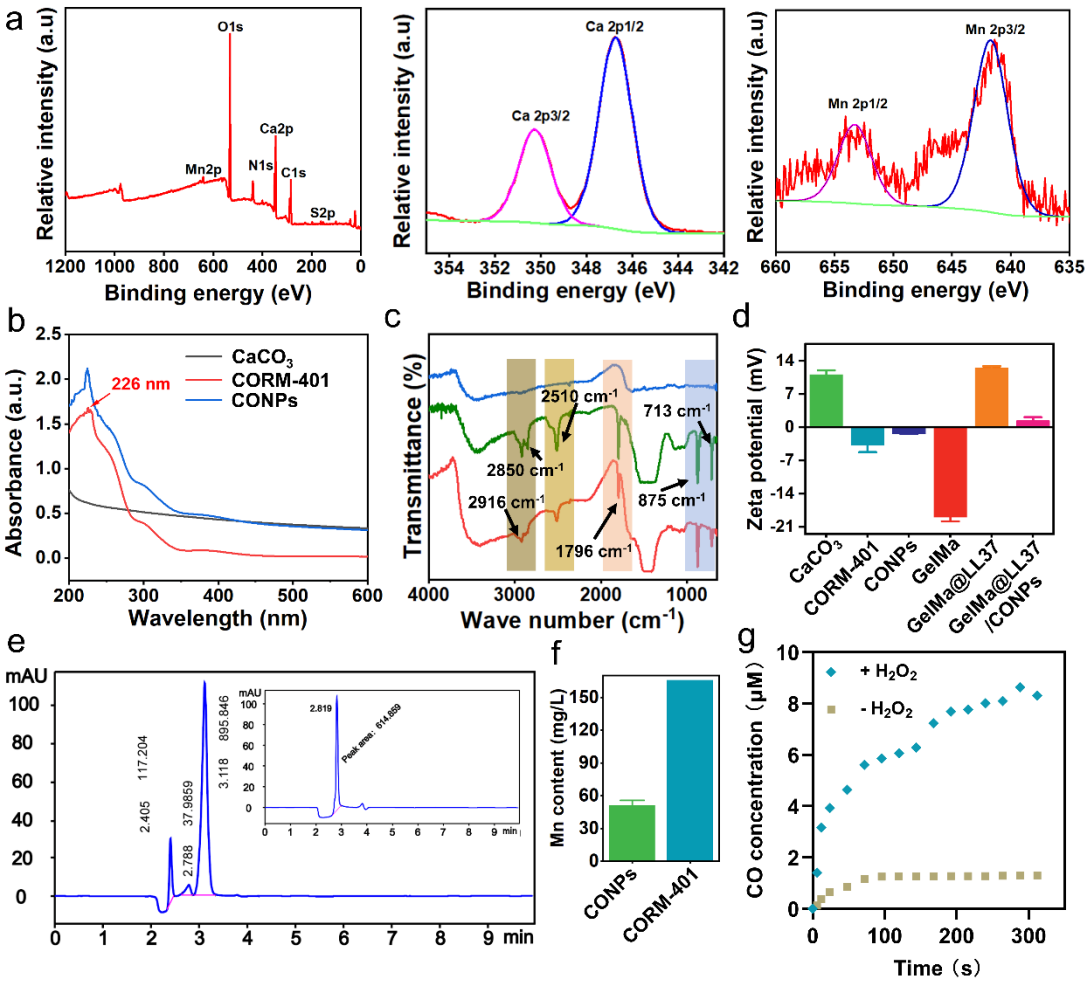


**Fig. 2 Physicochemical properties characterization of respiration-disrupted microspheres with in situ release of CO gas. a**, XPS patterns of CONPs. **b**, UV-Vis absorption spectra of $CaCO_3$, CORM-401 and CONPs. **c**, FTIR spectra of GelMa microspheres, $CaCO_3$ and GelMa@LL37/CONPs microspheres (order from top to bottom). **d**, Surface zeta potential of $CaCO_3$, CORM-401, CONPs, GelMa microspheres, GelMa@LL37 microspheres and GelMa@LL37/CONPs microspheres (n=3). **e**, The loading efficiency of LL37 in GelMa@LL37/CONPs microspheres and the corresponding position and area of LL37 antimicrobial peptide are 3.118 min and 895.846 mAU, respectively. The image inserted in the upper right corner shows the LL37 antimicrobial peptide standard, and the peak position and area are 2.819 min and 614.86 mAU, respectively. **f**, The loading efficiency of CROM-401 (Mn element concentration, n=3). **g**, CO release capacity of GelMa@LL37/CONPs microspheres with or without $H_2O_2$.

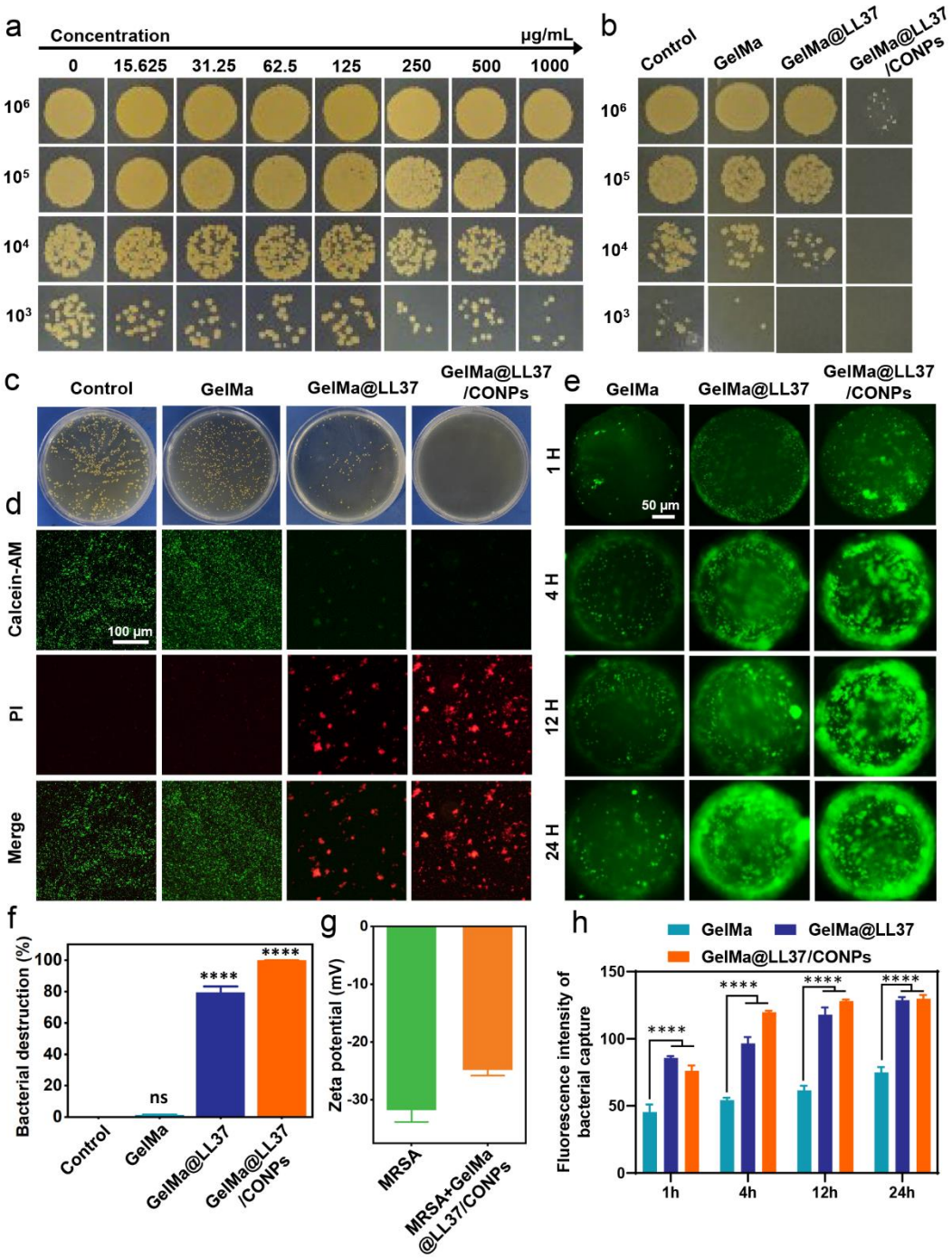


**Fig. 3 In situ release of CO gas from respiratory disrupting microspheres to capture bacteria. a**, Effective concentration evaluation of 0-1000 μg/mL LL37 antimicrobial peptide to kill MRSA bacteria. **b-d**, Colony counts (**b**,**c**) and live-dead staining (**d**) of MRSA bacteria after treatment with Control, GelMa microspheres, GelMa@LL37 microspheres and GelMa@LL37/CONPs microspheres. **e**,**h**, Fluorescence pictures (**e**) and fluorescence intensity analysis (**h**) of GelMa microspheres, GelMa@LL37 microspheres and GelMa@LL37/CONPs microspheres

capturing MRSA bacteria at different time points (n=3). **f**, Bactericidal efficiency of Control, GelMa microspheres, GelMa@LL37 microspheres and GelMa@LL37/CONPs microspheres (n=3). **g**, Surface zeta potential of GelMa@LL37/CONPs microspheres treated with MRSA (n=3). (****$p < 0.0001$)

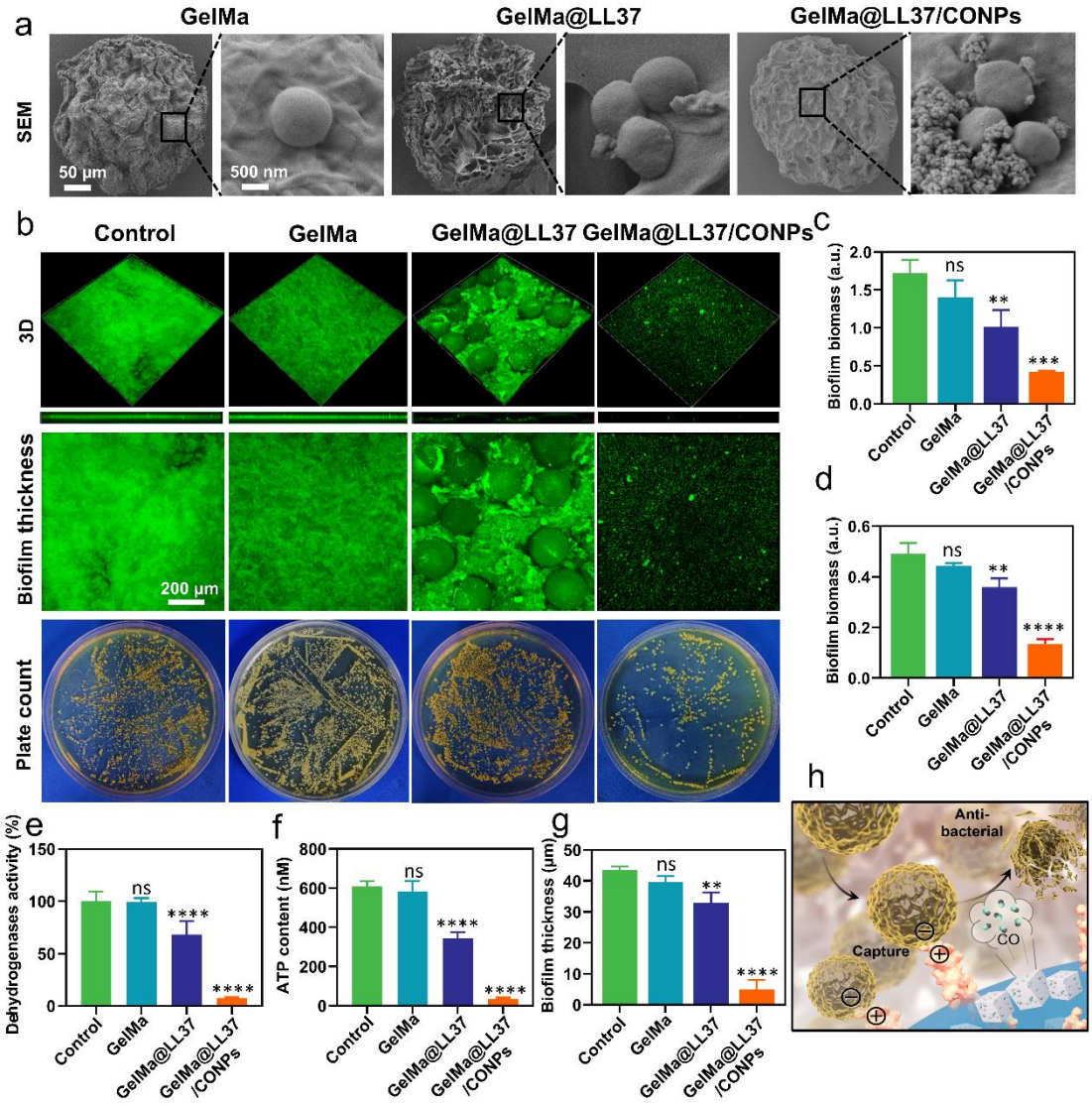


**Fig. 4 Bacterial respiration disruption microspheres release CO gas disrupting the MRSA biofilm ecotone**. **a**, SEM images of bacterial viability on the surface of GelMa, GelMa@LL37 and GelMa@LL37/CONPs microspheres. **b-d**, Laser confocal images (**b**), and OD values of bacterial numbers (**c**) and crystalline violet staining (**d**) of MRSA biofilms treated with GelMa, GelMa@LL37 and GelMa@LL37/CONPs microspheres (n=3). **e-g**, Quantitative analysis of dehydrogenases activity (**e**), ATP content (**f**) and biofilm thickness (**g**) (n=3). **h**, Schematic diagram of GelMa@LL37/CONPs microspheres removing MRSA biofilms (*p < 0.05, ****p < 0.0001).

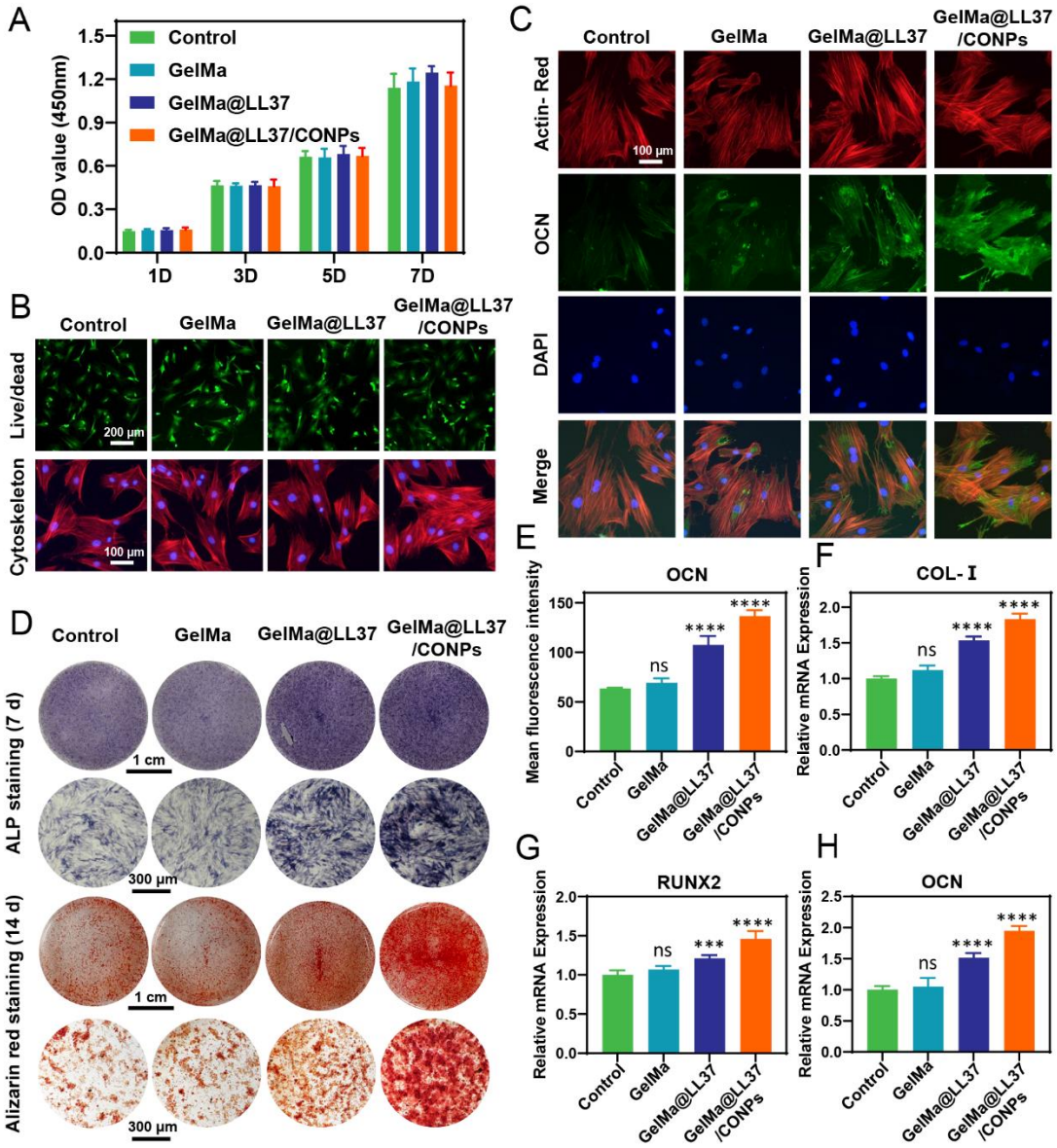


**Fig. 5 Cytological evaluation of bacterial respiratory disruption microspheres.** **a**,**b**, CCK-8 method (**a**), Live dead staining and skeletal staining (**b**) to assess the cell viability of BMSCs after GelMa, GelMa@LL37 and GelMa@LL37/CONPs microspheres treatment. **c-f**, GelMa, GelMa@LL37 and GelMa@LL37/CONPs microspheres treatment of BMSCs after OCN immunofluorescence expression (**c**) and ALP, alizarin red staining (**d**) quantitative calculation of OCN immunofluorescence intensity (**e**). **f-h**, Relative expression of COL-I(**f**), RUNX2 (**g**) and OCN genes (**h**) after GelMa, GelMa@LL37 and GelMa@LL37/CONPs microspheres treatment of BMSCs (n=3, ***p < 0.001, ****p < 0.0001).

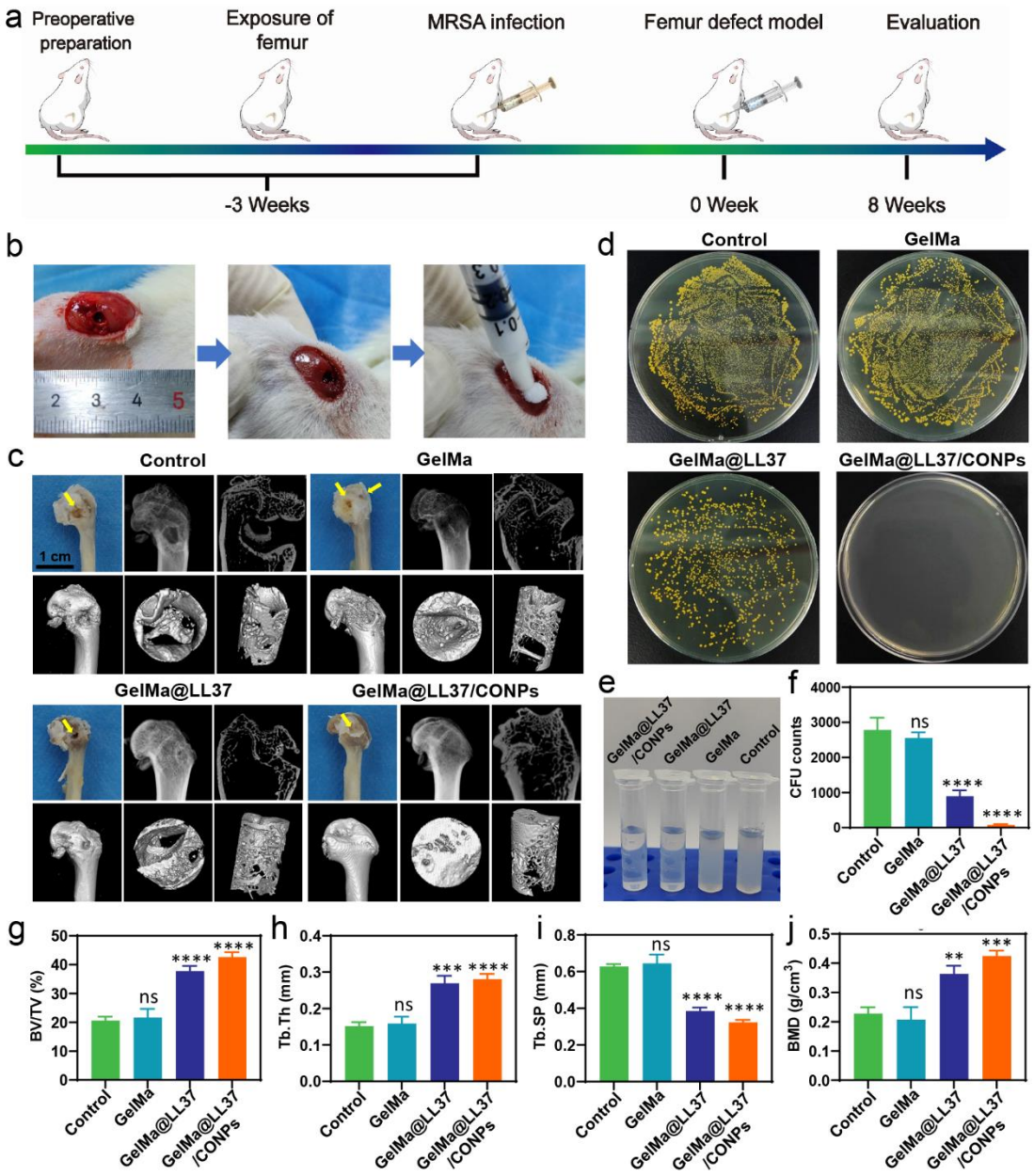


**Fig. 6 Bacterial respiratory disruption of microspheres for *in vivo* clearance of MRSA biofilm. a**, Construction and treatment procedure of the osteomyelitis model. **b**, Surgical procedure and material implantation. **c**, Optical images, X-ray and Micro-CT reconstructions of bone infection sites after 8 weeks of GelMa, GelMa@LL37 and GelMa@LL37/CONPs microspheres filling; **d-f**, Bacterial survival status at the site of bone infection after GelMa, GelMa@LL37 and GelMa@LL37/CONPs microspheres treatment. **g-j**, BV/TV (**g**), Tb.Th (**h**), Tb.SP (**i**) and BMD (**j**) in GelMa, GelMa@LL37 and GelMa@LL37/CONPs microspheres treatment groups (n=3, **p < 0.01, ***p < 0.001, ****p < 0.0001).

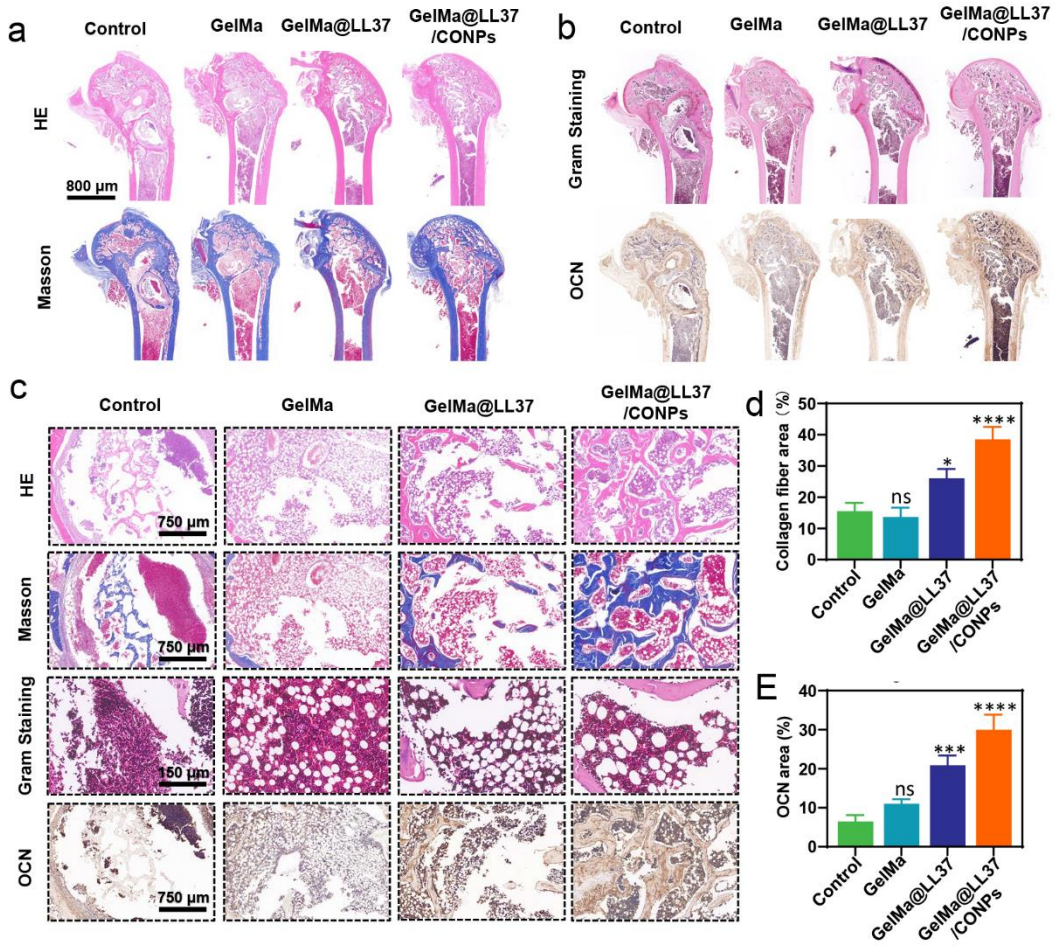


**Fig. 7** ***In vivo*** **histological evaluation of bacterial respiratory disruption microspheres. a-c**, HE, Masson (**a**), Gram and OCN staining (**b**) of the GelMa, GelMa@LL37 and GelMa@LL37/CONPs microspheres groups and their magnified images (**c**). **d**,**e**, Collagen fiber area (**d**) and immunohistochemical OCN expression (**e**) area of GelMa, GelMa@LL37 and GelMa@LL37/CONPs microspheres treatment groups (n=3, *p < 0.05, **p < 0.01, ***p < 0.001, ****p < 0.0001)